Inorganic Chemistry

Article

pubs.acs.org/IC

# A General Approach to Spindle-Assembled Lanthanide Borate Nanocrystals and Their Photoluminescence upon $Eu^{3+}$/$Tb^{3+}$ Doping

Yubin Zeng, Zhengquan Li,* Yingfang Liang, Xiaoqin Gan, and Mengmeng Zheng

Department of Materials Physics, Zhejiang Normal University, Jinhua, Zhejiang 321004, People's Republic of China

S *Supporting Information*

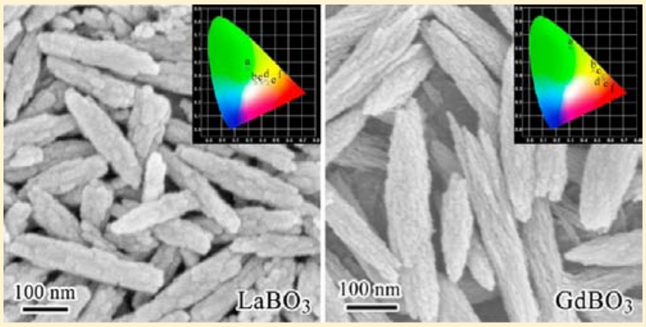

**ABSTRACT:** Uniform-assembled lanthanide borate nanocrystals have been synthesized via a facile self-assembly process under hydrothermal conditions. All of the prepared lanthanide borate assemblies exhibit a spindle-like profile despite the fact that they belong to different crystal systems and have different formulas for composition. Each assembly is composed of small nanocrystals that are tightly attached along with their lateral surfaces. X-ray diffraction, scanning electron microscopy, and transmission electron microscopy have been used to characterize the structure and morphology of these samples. The mechanism responsible for the growth and assembly of these lanthanide borate assemblies is also demonstrated. After $Eu^{3+}$ and/or $Tb^{3+}$ ions are doped inside these assemblies, strong and multicolor emissions can be realized. Notably, tunable emission and a warm-white color can be achieved in the $Eu^{3+}$/$Tb^{3+}$ codoped samples.

## 1. INTRODUCTION

Nowadays, nano/microstructures with well-defined shapes and architectures have attracted considerable interest because their chemical and physical properties are closely associated with their geometrical factors such as size, dimensionality, morphology, and orientation.[1−3] Generally, inorganic nanomaterials with similar structural characteristics can show some common properties and generate many unique applications. For example, hollow and porous nano/microstructures have a large surface area for adsorption and thus have been widely used in drug delivery.[5,6] One-dimensional metal nanowires show excellent electronic transportation properties and have been employed as interconnectors in microscale devices.[7] To develop various nanostructures with the same architecture, a template method is generally preferred because different types of crystals have different growth habits, which easily lead to diverse morphologies.[4,8] Due to the lack of templates, however, this method is limited to the synthesis of a few nanostructures such as hollow spheres, nanorods, nanowires, etc. The self-assembly of nanocrystals during their growth or mature stage can provide another solution to developing complicated nano/microarchitectures.[9−11] The tiny nanocrystals can, in principle, combine to form various kinds of geometries if the attachment of nanocrystals could be freely directed. To date, many complex microstructures have been synthesized based on the self-assembly process.[9−11] However, it is worth noting that the preparation conditions for a targeting architecture in different materials are varied from case to case, because the growth and assembly of nanocrystals strongly depend on the crystalline phases, compositions, and growth habits of the nanocrystals. It remains a grand challenge to synthesize a series of nano/microstructures in a similar hierarchical architecture regardless of their crystalline phases and compositions.

Nanocrystals of lanthanide compounds have received increasing attention because of their unique optical, electronic, and magnetic properties arising from the 4f electrons, which enable their wide applications in high-performance phosphors, magnetic resonance imaging, and biological labels.[12−15] Among these nanocrystals, lanthanide borates ($LnBO_3$) are attractive to research communities because of their high stability, strong luminescence, excellent vacuum ultraviolet (VUV) transparency, and exceptional optical damage thresholds.[16−21] $LnBO_3$ has been proven to be an excellent host matrix for the luminescence of $Eu^{3+}$ and $Tb^{3+}$, respectively, and widely used in luminescent devices.[16−21] Controlled synthesis of $LnBO_3$ nano/microcrystals has been attempted, and a few conventional structures have been developed such as $TbBO_3$ microspheres, $LuBO_3$ microplates, and $YBO_3$ drumlike crystals.[16−18] Despite this progress, a general method to obtain various $LnBO_3$ nanocrystals that are arranged with a similar architecture is still lacking. Furthermore, little attention has been paid to the synthesis of $LnBO_3$ nanocrystals with large $Ln^{3+}$ ions (e.g., $La^{3+}$, $Pr^{3+}$, and $Nd^{3+}$) that generally possess an orthorhombic or a monoclinic phase instead of a hexagonal one, while it is known that luminescence of a $Eu^{3+}$ ion is much more sensitive to the crystalline phase of a crystal.[22,23]

In this work, we present a hydrothermal approach to synthesizing various lanthanide (La−Tb) borate nanocrystals that are self-assembled into a three-dimensional architecture.

**Received:** May 24, 2013
**Published:** July 30, 2013

These assemblies exhibit a spindle-like appearance, and each of them consists of many tiny lanthanide borate nanocrystals. Although each of the prepared samples is pure in phase, they belong to three different crystal systems (i.e., orthorhombic, monoclinic, and hexagonal). To our surprise, these samples display similar morphology regardless of their differences in crystalline phases and compositions. Lanthanide borate nanocrystals with large $Ln^{3+}$ ions that belong to nonhexagonal systems are also prepared, providing a good platform for the investigation of $Eu^{3+}$ luminescence in different crystalline phases but with similar morphology. After being doped with $Tb^{3+}$ and $Eu^{3+}$ ions, these lanthanide borate assemblies can give strong photoluminescence, suggesting that they are good host matrixes for lanthanide doping. Through codoping of $Eu^{3+}$ and $Tb^{3+}$ ions and changing of the doping ratio, we obtain tunable emissions in the codoped lanthanide borate samples in either an orthorhombic or a hexagonal phase. Furthermore, a warm-white color has been realized in the codoped sample by tuning the ratio of $Tb^{3+}/Eu^{3+}$ to a certain value. It is anticipated that this work can shed new light on the synthesis and self-assembly of lanthanide nanocrystals. In comparison with randomly dispersive luminescent nanocrystals, the assembled nanocrystals in a single-particle form can locally enhance the fluorescence and improve their performance on the single-particle basis, which may be implemented as a single function spot in future color displays or biolabels.

## 2. EXPERIMENTAL SECTION

**2.1. Syntheses of Spindle Assemblies of Lanthanide Borate Nanocrystals.** All of the reagents were purchased from Sinopharm Chemical Reagents Co. Ltd. and used without further purification. Using the synthesis of $TbBO_3$ spindle assemblies as an example, 2 mmol of $TbCl_3$ powder was dissolved in 20 mL of deionized (DI) water, followed by the addition of an aqueous NaOH solution (10 mL, 0.5 M) to form $Tb(OH)_3$ colloids. Subsequently, 15 mL of an aqueous poly(vinylpyrrolidone) (PVP; MW = 30000, 0.448 g) solution and 0.26 g of a $H_3BO_3$ powder were added into the solution and stirred for 30 min. The mixed solution was then transferred to a 50 mL Teflon-line autoclave and sealed. The autoclave was heated to 200 °C and maintained at this temperature for 24 h. After naturally cooling down to room temperature, the products were collected by centrifugation at a speed of 3000 rpm for 10 min. The products were then washed with ethanol and DI water twice and finally dried in a vacuum at 80 °C. Other lanthanide borate assemblies were prepared with a similar procedure except using different lanthanide chlorides instead of $TbCl_3$ in the first step. Lanthanide-doped (i.e., $Eu^{3+}/Tb^{3+}$) products were obtained through the same procedure by introducing a stoichiometric amount of dopants (other lanthanide chlorides) into the original chloride solution.

**2.2. Characterizations.** Powder X-ray diffraction (XRD) was carried out on a Philips X'Pert Pro X-ray diffractometer equipped with Cu K$\alpha$ radiation. Scanning electron microscopy (SEM) images were obtained by a Hitachi S-4800 field-emission scanning electron microscope. Transmission electron microscopy (TEM) images were recorded on a JEOL 2100F transmission electron microscope. The TEM samples were prepared by dropping a suspension of assemblies on a carbon-film-coated copper grid. Fluorescence spectra were acquired on an Edinburgh FLS920 spectrometer equipped with a xenon lamp.

## 3. RESULTS AND DISCUSSION

**3.1. Phase and Morphology of the Prepared Lanthanide Borate Assemblies.** XRD patterns have been used to characterize the phase of as-obtained lanthanide nanocrystals, and the data from eight samples are shown in Figure 1. It is found that four types of phases appear among these samples, judging from the positions of their XRD peaks (see Figure S1 in the Suppporting Information, SI). The $LaBO_3$ sample (Figure 1A) can be clearly indexed to a pure $LaBO_3$ crystal in an orthorhombic phase (JCPDS no. 08-0193). As for the praseodymium and neodymium samples (Figure 1C,D), all of the peaks match well with the lanthanide metaborate crystals in a monoclinic phase (JCPDS nos. 23-1385 and 23-1260), which can be formulated as $Pr_2(BO_2)_3$ and $Nd_2(BO_2)_3$. XRD peaks from the $SmBO_3$, $EuBO_3$, $GdBO_3$, and $TbBO_3$ samples are much more similar, suggesting that they have the same crystalline structures (Figure 1E−H). Through careful indexing, each pattern can be assigned to pure lanthanide orthoborate crystals in a hexagonal phase (JCPDS nos. 74-1930, 13-0485, 74-1932, and 24-1272). Obviously, the above results indicate that three kinds of phases are obtained in these lanthanide borate samples even although they are prepared with the same method. The difference in the phases of these samples probably resulted from lanthanide contraction, namely, a decrease in the ionic radii in the lanthanide series. As such, smaller ions favor the hexagonal phase in the borate samples, while the bigger ones prefer the monoclinic phase and the biggest one chooses the orthorhombic phase. In the case of the preparation of cerium borate, only pure cubic $CeO_2$ was obtained under the same experimental conditions (JCPDS no. 81-0792). This result can be attributed to the instability of $Ce^{3+}$ ions because they are easily oxidized to $Ce^{4+}$ in the hydrothermal conditions and unable to further react with borate ions.

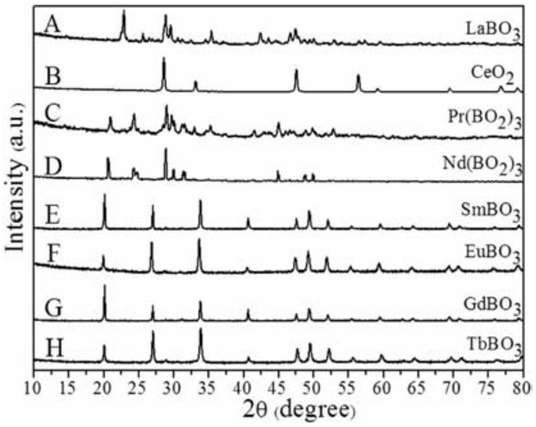

**Figure 1.** XRD patterns of the prepared lanthanide samples. Each pattern can be clearly indexed to the JCPDS data in a pure phase, respectively.

Morphologies of the prepared samples were examined by SEM and are shown in Figure 2. An overview of the SEM images shows that all of the prepared samples are uniform in size with narrow size distribution. Except that the $CeO_2$ particles are spherical in shape, all of the lanthanide borate samples display a spindle-like appearance despite the fact that they belong to different crystal systems. The surface of these spindle particles is rough, implying that they are not single crystals. The diameters of these particles are about 80−200 nm, and their lengths vary from 550 to 900 nm. Magnified SEM images indicate that a single spindle particle is constituted by many small nanocrystals that are tightly attached together. Some component nanocrystals exhibit a rod shape with a diameter of 10−30 nm and a length of 20−50 nm (see Figure S2 in the SI).

Table 1 summarizes the crystal structures, space groups, morphologies, diameters, lengths, and aspect ratios of these

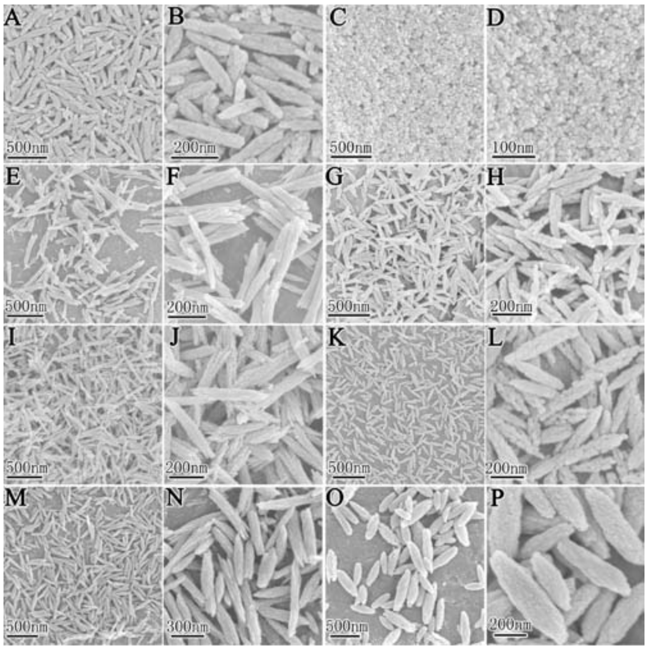

**Figure 2.** SEM images of the prepared lanthanide samples: (A and B) $LaBO_3$; (C and D) $CeO_2$; (E and F) $Pr(BO_2)_3$; (G and H) $Nd(BO_2)_3$; (I and J) $SmBO_3$; (K and L) $EuBO_3$; (M and N) $GdBO_3$; (O and P) $TbBO_3$.

**Table 1. Summary of the Phases and Morphological Features of the Prepared Lanthanide Assemblies**

| products | phase | morphology | diameter (nm) | length (nm) | aspect ratio |
|---|---|---|---|---|---|
| $LaBO_3$ | orthorhombic | spindle | 82 | 550 | 6.71 |
| $Pr(BO_2)_3$ | monoclinic | spindle | 83 | 531 | 6.40 |
| $Nd(BO_2)_3$ | monoclinic | spindle | 85 | 491 | 5.78 |
| $SmBO_3$ | hexagonal | spindle | 90 | 456 | 5.10 |
| $EuBO_3$ | hexagonal | spindle | 113 | 498 | 4.40 |
| $GdBO_3$ | hexagonal | spindle | 180 | 725 | 4.03 |
| $TbBO_3$ | hexagonal | spindle | 254 | 896 | 3.52 |

lanthanide borate particles. It can be seen from the table that the diameters of these spindle particles increase along with a decrease of the ionic radii from $La^{3+}$ to $Tb^{3+}$.[30−33] Accordingly, the aspect ratios of these particles gradually decrease in the same manner. For example, $LaBO_3$ particles have an aspect ratio of 6.71, and that of $TbBO_3$ particles has been reduced to 3.52. It is also worth noting that orthorhombic $LaBO_3$ and monoclinic $Ln(BO_2)_3$ (Ln = Pr, Nd) particles are not as uniform as the hexagonal $LnBO_3$ (Ln = Sm−Tb) particles. This is presumably because orthorhombic and monoclinic crystals have relatively low symmetry compared to the hexagonal one, which may result in a few differences in nanocrystal growth and subsequent assembly. A similar phenomenon has also been observed in other lanthanide compounds reported elsewhere.[24]

To further investigate the structural features of these spindle particles, TEM was also employed to characterize their morphologies and herein we use $TbBO_3$ as an example. Figure 3 shows TEM images of $TbBO_3$ particles at different magnifications. From the low-magnification image (Figure 3A), one can see that each particle has a plump body and two slim ends, confirming their spindle geometries. Magnified TEM images (Figure 3B) indicate that one single particle consists of many small nanocrystals and the component nanocrystals are tightly attached together. Such a kind of assembly provides these particles uneven and rough surfaces, which is consistent with their SEM images (Figure 2O,P). A single $TbBO_3$ spindle particle and its corresponding selected area electron diffraction (SAED) pattern are shown in parts C and D of Figure 3, respectively. It is found that there are several dim circles and bright spots in the SAED pattern, implying that many component nanocrystals are arranged along a specific crystalline orientation, while the rest of them are attached randomly. The result may be induced by the oriented attachment of nanocrystals during maturation because it is a good way to reduce the surface energy.

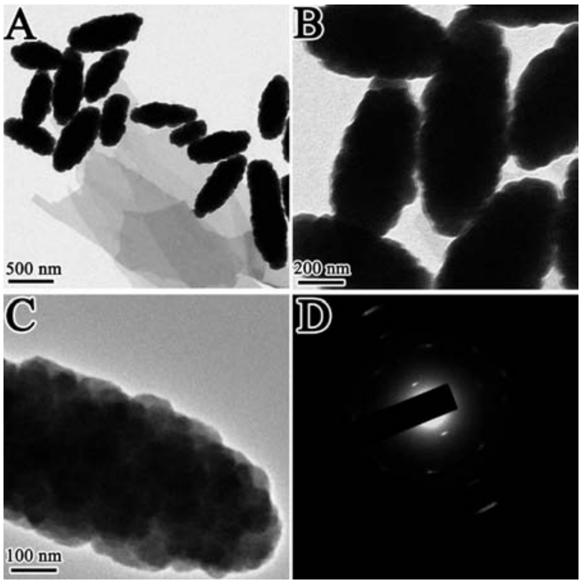

**Figure 3.** (A−C) TEM images of $TbBO_3$ assemblies at different magnifications. (D) Typical ED pattern of one single $TbBO_3$ assembly.

**3.2. Formation Mechanism of the Spindle-like Lanthanide Borate Assemblies.** To understand the formation mechanism, time-dependent experiments were carried out to study the morphological evolution of these spindle assemblies. Here we continue to use the formation of $TbBO_3$ spindle particles as an example. Figure 4 displays the SEM images of intermediate products obtained at different stages during a typical synthesis. When the reactants were mixed and kept in the autoclave for 3 h, many small nanoparticles were produced (Figure 4A). As the reaction proceeded for 6 h, some of the nanoparticles started to assemble into spindle-like structures (Figure 4B). When the reaction was prolonged for 6 h more, more and more nanoparticles were assembled into the spindle structures (Figure 4C). Finally, only spindle assemblies appeared when the time was prolonged for 24 h (Figure 4D). The above results clearly suggest that a typical self-assembly process is responsible for the formation of spindle assemblies.

The compositions of the intermediate products were also characterized by XRD and are shown in Figure 5. The results show that the product obtained at 3 h was a mixture of $Tb(OH)_3$ and $TbBO_3$ nanocrystals (Figure 5A). As the reaction proceeded, the $Tb(OH)_3$ nanocrystals were gradually transformed to $TbBO_3$ (Figure 5B), and only pure $TbBO_3$ was obtained after 12 h of reaction (Figure 5C,D). At the same time, we test the pH value of the raw solution. It is found that an obvious decrease in the pH value from 10 to 6.5 appears

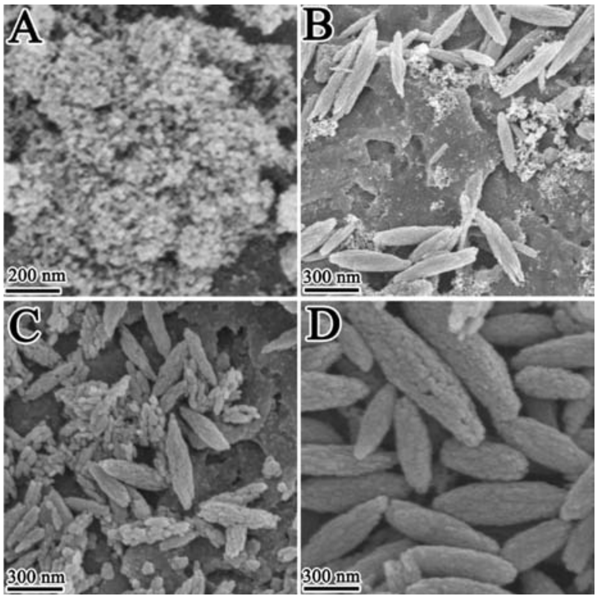

**Figure 4.** SEM images of intermediate samples during the synthesis of $TbBO_3$ assemblies collected at different time intervals: (A) 3 h; (B) 6 h; (C) 12 h; (D) 24 h.

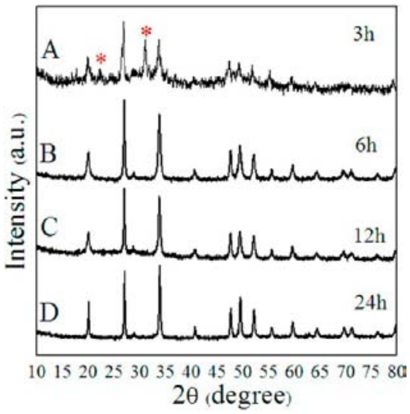

**Figure 5.** XRD patterns of intermediate samples during the synthesis of $TbBO_3$ assemblies collected at different time intervals: (A) 3 h; (B) 6 h; (C) 12 h; (D) 24 h.

from the beginning of the reaction and after 6 h, suggesting that the pH environment has oppositely changed during the synthesis.

On the basis of the above information, the mechanism responsible for the assembly process is proposed and illustrated in Figure 6. First, the detailed reactions can be described as follows:

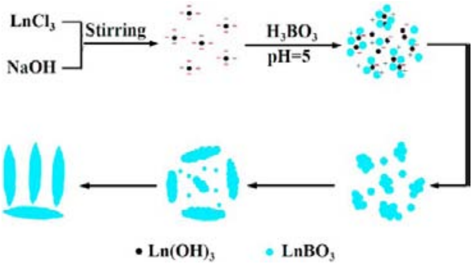

**Figure 6.** Schematic illustration of the growth and assembly mechanism of the spindle $LnBO_3$ assemblies.

$$TbCl_3 + 3NaOH \rightarrow Tb(OH)_3(s) + 3NaCl \tag{1}$$

$$H_3BO_3 \rightarrow BO_3{}^{3-} + 3H^+ \tag{2}$$

$$Tb(OH)_3(s) + BO_3{}^{3-} + 3H^+ \rightarrow TbBO_3(s) + 3H_2O \tag{3}$$

Reaction 1 produces $Tb(OH)_3$ colloids rapidly upon the addition of a NaOH solution, while reaction 3 is fairly slow because $H_3BO_3$ is a weak acid with low ionization in water. As a result, $Tb(OH)_3$ colloids are slowly transformed to $TbBO_3$ nanocrystals, and a mixture of them is produced before 6 h of reaction. Meanwhile, the pH of the solution is gradually changed because of continuous ionization of $H_3BO_3$. When the pH reaches a value below 7, the newly formed $TbBO_3$ nanocrystals will possess positive charges on their surface. These $TbBO_3$ nanocrystals have a tendency to attach surrounded $Tb(OH)_3$ colloids that were initially formed in basic conditions with a negatively charged surface. Such an electrostatic attraction will combine different nanocrystals, leading to the formation of assembled nanostructures. Once the residual $Tb(OH)_3$ colloids in these assemblies were completely transformed to $TbBO_3$, pure $TbBO_3$ spindle assemblies were obtained.

It should be noted that the slow transformation from $Ln(OH)_3$ to $LnBO_3$ plays a key role in producing the assembled nanostructures. Under the same hydrothermal process, we have also attempted the synthesis of other lanthanide borates (from Dy to Lu) in a hexagonal phase. It was found that $LuBO_3$ spindle assemblies can be successfully obtained, while free nanoparticles were produced in other samples. This result is probably attributed to the fact that the transformation from $Ln(OH)_3$ to $LnBO_3$ (Ln = Dy, Ho, Y, Er) is faster than other lanthanide samples under the given conditions, according to their XRD data in the intermediate samples. As such, pure lanthanide borates were quickly formed that could not self-assemble because they possess the same surface charges.

The assembly process is independent of the inherent crystal structures of these samples because three kinds of crystalline phases have no obvious common structural characteristics. In addition to the crystal structures, the surface and size effects of nuclei are also found to be effective knobs to obtaining the assembled nanostructures in recent years.[25] In our case, specifically, the surface charge plays the key role in inducing the initial assembly of nanocrystals rather than other parameters such as sizes and surfactants. Once the nanocrystals are attached, the maturation of these spindle particles is then processed through the oriented attachment of surrounding nanocrystals and/or Oswald ripening process.

**3.3. Effect of the Surfactants.** Surfactants can adhere to the surface of nanocrystals during crystal growth; thus, they can play an important role in controlling the size and morphology of the final nanocrystals.[26−28] To investigate the function of surfactant PVP in our synthesis, control experiments without or with different surfactants were carried out. Figure 7 shows the SEM images of four prepared $TbBO_3$ samples. Without any surfactant, the sample is big platelike particles, and each particle is piled up by several thin and round plates (Figure 7A). Such a morphology may be attributed to the growth habit of $TbBO_3$ crystals, which prefer to grow along two lateral directions rather

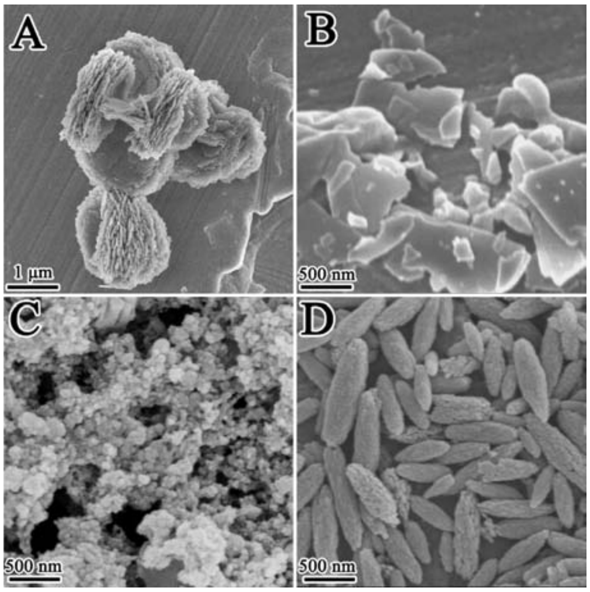

Figure 7. SEM images of the $TbBO_3$ samples obtained without or with different surfactants: (A) no surfactant; (B) 4 mmol of CTAB; (C) 4 mmol of SDS; (D) 4 mmol of PVP.

than the vertical one. As such, thin plates were formed and piled layer-by-layer in order to reduce their surface energies. This result is consistent with the previous reports.[17] When sodium dodecyl sulfate (SDS) or cationic surfactant cetyltrimethylammonium bromide (CTAB) was employed, irregular particles were obtained, showing that the ionic surfactant can greatly affect the growth and assembly of the final nanocrystals (Figure 7B,C). This is due to the fact that anionic surfactants can strongly bind to the surface-charged intermediate colloids, either $Tb(OH)_3$ or $TbBO_3$.[26−28] SDS prefers to adhere to positively charged $TbBO_3$ colloids and impede the assembly tendency, so that dispersive nanocrystals rather than assembled ones were formed. In the same manner, CTAB chooses to bind negatively charged $Tb(OH)_3$ colloids at the beginning of the synthesis. After positively charged $TbBO_3$ nanocrystals were formed, severely agglomerate particles were produced.

In contrast, PVP is a nonionic surfactant and is insensitive to the surface charge of nanocrystals. It only regulates the growth rates of different crystal planes through selective surface adsorption.[29] Compared to the sample obtained without surfactant, we can infer that PVP can efficiently prohibit the growth habit of forming plate $TbBO_3$ crystals through reduction of the growth rates of two lateral planes. The slow growth of nanocrystals under PVP results in small $TbBO_3$ nanocrystals, providing suitable building units for the spindle hierarchical particles. At the same time, PVP also provides a controlled environment for nanoparticle assembly, which favors the formation of uniform particles (Figure 7D).

**3.4. Photoluminescence (PL) Properties.** Various luminescent lanthanide ions have been successfully doped inside these spindle $LnBO_3$ assemblies, and their PL properties are investigated. Figure 8 shows the PL spectra of $Eu^{3+}$- or $Tb^{3+}$-doped samples using $LaBO_3$ and $GdBO_3$ as the host matrixes, respectively. Under excitation of a 285 nm wavelength, the $Eu^{3+}$-doped assemblies (Figure 8A,C) exhibit a group of emissions mainly located at 580, 592, 613, 650, and 699 nm, which are attributed to the $^5D_0 \rightarrow {}^7F_J$ ($J = 0, 1, 2, 3, 4$) transitions of $Eu^{3+}$ ions.[28,29] The PL spectra of the $Tb^{3+}$-doped sample (Figure 8B,D) show a strong emission at 545 nm and three weak emissions at 488, 588, and 624 nm, which are

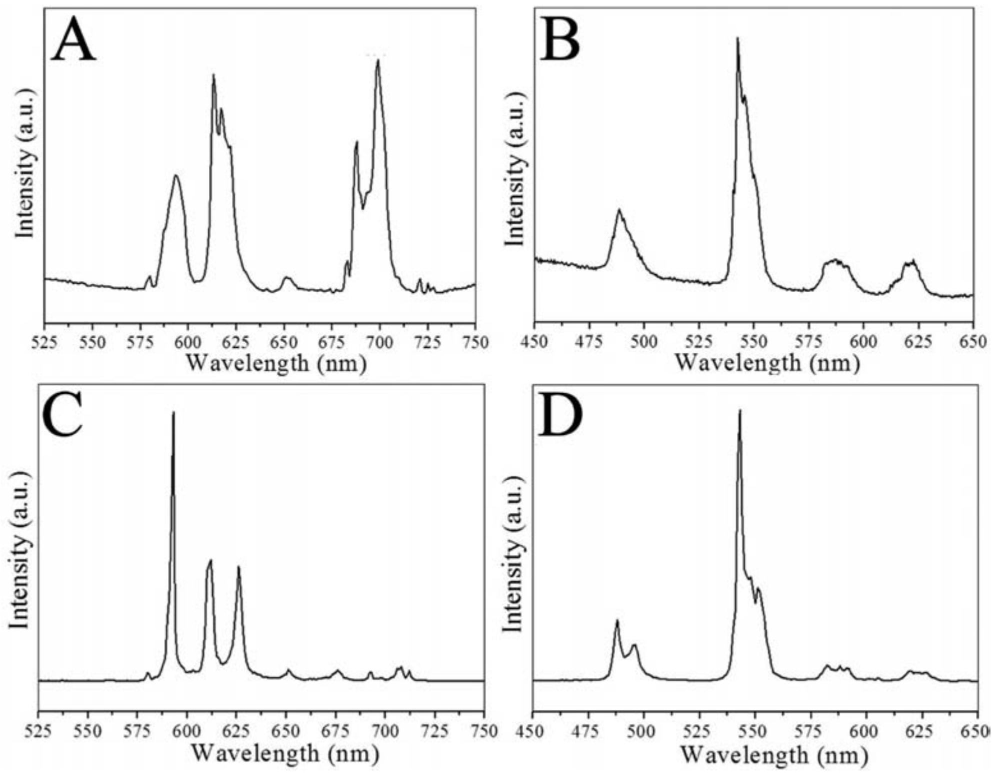

Figure 8. PL spectra of the $Eu^{3+}$ or $Tb^{3+}$ singly doped samples using different assemblies as host matrixes: (A) $LaBO_3:Eu^{3+}$; (B) $LaBO_3:Tb^{3+}$; (C) $GdBO_3:Eu^{3+}$; (D) $GdBO_3:Tb^{3+}$. The excitation wavelength is 285 nm in all of the samples.

ascribed to the $^5D_4 \rightarrow {}^7F_J$ ($J$ = 6, 5, 4, 3) transitions of $Tb^{3+}$ ions.[17,21] Note that the relative intensity and width of the emission peaks in the $LaBO_3:Eu^{3+}$ sample (Figure 8A) are tremendously different from those in the $GdBO_3:Eu^{3+}$ sample (Figure 8C). The emissions in $LaBO_3:Eu^{3+}$ are broad, and the $^5D_0 \rightarrow {}^7F_2$ and $^5D_0 \rightarrow {}^7F_4$ transitions are stronger than the $^5D_0 \rightarrow {}^7F_1$ transition. In the $GdBO_3:Eu^{3+}$ sample, however, the same emissions are much more narrow. The $^5D_0 \rightarrow {}^7F_1$ transition is twice as strong as the $^5D_0 \rightarrow {}^7F_2$ transition, and the $^5D_0 \rightarrow {}^7F_4$ transition almost decreases to zero. In contrast, the PL spectrum of $Tb^{3+}$-doped $LaBO_3$ (Figure 8B) has no significant difference from that of $Tb^{3+}$-doped $GdBO_3$ (Figure 8D). The green emission from the $^5D_4 \rightarrow {}^7F_5$ transition is dominant in both samples. Monoclinic $Pr_2(BO_2)_3:Eu^{3+}$ and $Nd_2(BO_2)_3:Eu^{3+}$ samples show a relatively weak fluorescence, and their peaks are similar to those of $LaBO_3:Eu^{3+}$ because of their asymmetrical crystalline structures. A detailed spectral investigation and discussion about them are not presented here.

In the $Eu^{3+}$-doped samples, it is known that $^5D_0 \rightarrow {}^7F_1$ belongs to a magnetic dipole transition while $^5D_0 \rightarrow {}^7F_2$ and $^5D_0 \rightarrow {}^7F_2$ originate from electric dipole transitions.[23] The intensity of an electric dipole transition depends strongly on the site symmetry of a crystal, while that of a magnetic dipole transition is not affected by it. On the basis of the Judd−Ofelt theory, electric dipole transitions will be dominant if the $Eu^{3+}$ ions occupy the sites without inversion symmetry.[32,33] In our samples, the $Eu^{3+}$ ions doped in an orthorhombic lattice have less inversion symmetry than the ones doped in a hexagonal lattice. Therefore, electric dipole transitions of $^5D_0 \rightarrow {}^7F_2$ and $^5D_0 \rightarrow {}^7F_4$ will no longer be forbidden in the $LaBO_3$ assemblies. As such, $LaBO_3:Eu^{3+}$ assemblies can show strong red and near-IR emissions simultaneously, while the $GdBO_3:Eu^{3+}$ assemblies only give three characteristic orange emissions. The emissions from $Tb^{3+}$-doped samples are not sensitive to the crystal structures; thus, no obvious difference is found between orthorhombic $LaBO_3:Tb^{3+}$ and hexagonal $GdBO_3:Tb^{3+}$ assemblies.

Because both $Tb^{3+}$- and $Eu^{3+}$-doped samples can be excited at an identical wavelength (285 nm), $Tb^{3+}$ and $Eu^{3+}$ ions can be, in principle, codoped inside the $LnBO_3$ assemblies. These codoped materials may realize tunable multicolor emissions and have practical applications in color displays, fluorescent lamps, and LEDs. We have prepared a series of samples, among which different ratios of $Eu^{3+}/Tb^{3+}$ were codoped (total: 5 mol %). Owing to the difference in $Eu^{3+}$ emissions, herein we used the $LaBO_3$ and $GdBO_3$ assemblies to demonstrate this concept (Figures 9 and 10). Under excitation of 285 nm, red emissions will gradually increase with an increase of the $Eu^{3+}$ concentration in the $LaBO_3$ assemblies (from part A to part F in Figure 9). Meanwhile, green emissions also gradually rise along with an increase of the $Tb^{3+}$ concentration (from part F to part A in Figure 9). The relative intensities of the green and red emissions can be controlled by the doping ratio of $Eu^{3+}/Tb^{3+}$. Both strong green and red emissions are observed in the codoped samples with moderate concentrations of $Eu^{3+}$ and $Tb^{3+}$. A similar result is also found in the codoped $GdBO_3$ assemblies (Figure 10).

On the basis of the emission spectra of $Eu^{3+}/Tb^{3+}$-codoped $LaBO_3$ and $GdBO_3$ assemblies, a corresponding CIE chromaticity diagram can be plotted (Figure 11). The colors of these samples are marked according to their $x$ and $y$ coordinates, respectively. In both types of host matrixes, the color of these samples can be finely tuned from green, yellow, and orange to red by changing the doping ratio of $Eu^{3+}/Tb^{3+}$. These results indicate that the prepared samples can exhibit multicolor emissions in the visible region when excited under a single excitation wavelength. Among these samples, the 3% $Eu^{3+}$- and 2% $Tb^{3+}$-codoped $LaBO_3$ assemblies have coordinates of $x = 0.355$ and $y = 0.350$, which are close to the standard white-light color ($x = 0.333$, $y = 0.333$). This material can be potentially applied in the white LED lamps by coupling with a UV chip.

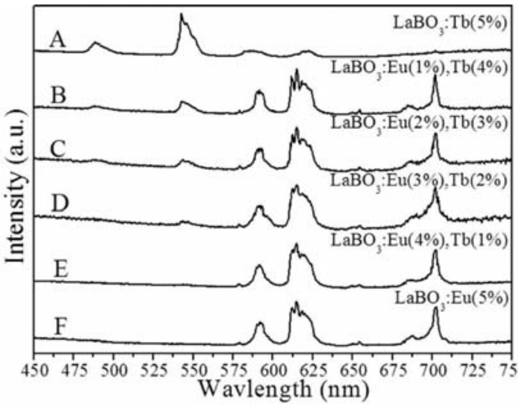

**Figure 9.** PL spectra of the $Eu^{3+}/Tb^{3+}$-codoped $LaBO_3$ assemblies with different doping ratios: (A) 0% Eu, 5% Tb; (B) 1% Eu, 4% Tb; (C) 2% Eu, 3% Tb; (D) 3% Eu, 2% Tb; (E) 4% Eu, 1% Tb; (F) 5% Eu, 0% Tb. The excitation wavelength is 285 nm.

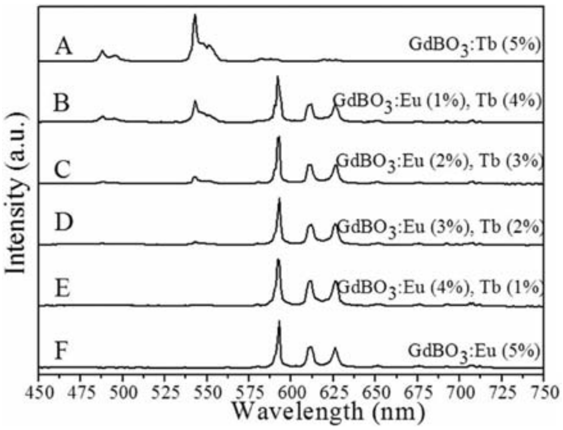

**Figure 10.** PL spectra of the $Eu^{3+}/Tb^{3+}$-codoped $GdBO_3$ assemblies with different doping ratios: (A) 0% Eu, 5% Tb; (B) 1% Eu, 4% Tb; (C) 2% Eu, 3% Tb; (D) 3% Eu, 2% Tb; (E) 4% Eu, 1% Tb; (F) 5% Eu, 0% Tb. The excitation wavelength is 285 nm.

## 4. CONCLUSIONS

In summary, a facile hydrothermal approach has been developed for the synthesis of various lanthanide (La−Tb) borate nanocrystals. All of the prepared lanthanide assemblies display similar spindle-like architecture despite the fact that they belong to three different crystal systems. Each of the assemblies is constituted by many small nanocrystals that attached together with their lateral surface. The formation mechanism responsible for the spindle assemblies has been demonstrated. After being doped with $Eu^{3+}$ and $Tb^{3+}$, respectively, these lanthanide assemblies can show strong fluorescence and crystalline structure-dependent emissions of $Eu^{3+}$ ions have been studied using different-phased samples as

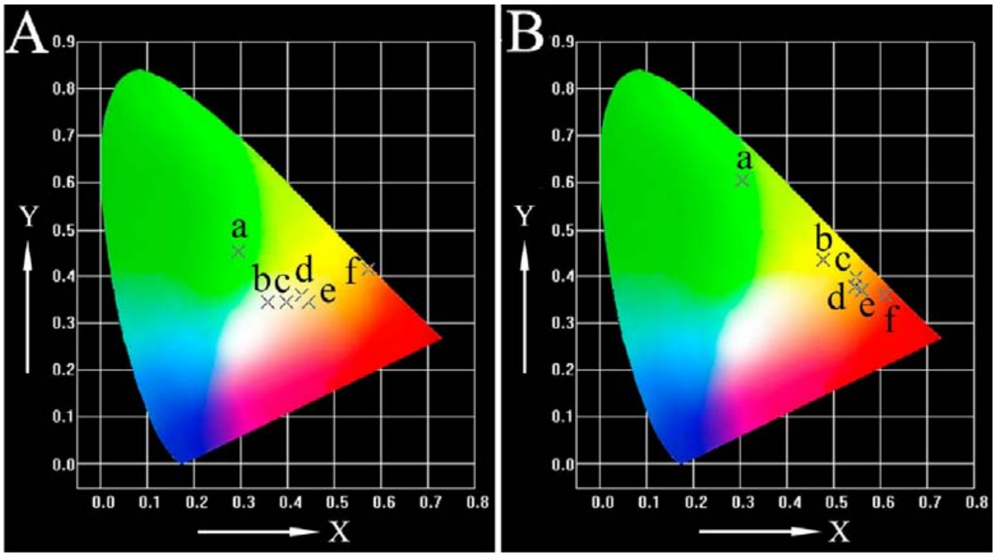

**Figure 11.** CIE chromaticity diagram of the emission spectra from the $Eu^{3+}/Tb^{3+}$-codoped $LaBO_3$ assemblies (A) and $GdBO_3$ assemblies (B). Marks a−f in the two images correspond to the spectra from samples A to F in Figures 9 and 10, respectively.

host matrixes. Tunable emissions have been achieved by the codoping of $Eu^{3+}$ and $Tb^{3+}$ in these assemblies with different doping ratios. A warm-white color can be realized in the $LaBO_3$-codoped assemblies. This new class of lanthanide borate phosphors with tunable emissions may find tremendous applications in future color displays, fluorescent lamps, and white LEDs.

## ■ ASSOCIATED CONTENT

### Ⓢ Supporting Information

XRD patterns and SEM and TEM images. This material is available free of charge via the Internet at http://pubs.acs.org.

## ■ AUTHOR INFORMATION

### Corresponding Author

*E-mail: zqli@zjnu.edu.cn.

### Notes

The authors declare no competing financial interest.

## ■ ACKNOWLEDGMENTS

The authors acknowledge financial support from the National Natural Science Foundation of China (Grant 21273203) and Natural Science Foundation of Zhejiang Province (Grant LY12B01001).

## ■ REFERENCES

(1) Xia, Y. N.; Xiong, Y. J.; Lim, B.; Skrabalak, S. E. *Angew. Chem., Int. Ed.* **2009**, *48*, 60.
(2) Liz-Marzan, L. M. *Langmuir* **2006**, *22*, 32.
(3) Jun, Y. W.; Chio, J. S.; Cheon, J. W. *Angew. Chem., Int. Ed.* **2006**, *45*, 3414.
(4) Lou, X. W.; Archer, L. A.; Yang, Z. C. *Adv. Mater.* **2008**, *20*, 3987.
(5) An, K. J.; Hyeon, T. *Nano Today* **2009**, *4*, 359.
(6) He, Q. J.; Shi, J. L. *J. Mater. Chem.* **2011**, *21*, 5845.
(7) Xia, Y. N.; Yang, P. D.; Sun, Y. G.; Wu, Y. Y.; Mayers, B.; Gates, B.; Yin, Y. D.; Kim, F.; Yan, H. Q. *Adv. Mater.* **2003**, *15*, 353.
(8) Wang, Y. J.; Angelatos, A. S.; Caruso, F. *Chem. Mater.* **2008**, *20*, 848.
(9) Zeng, H. C. *J. Mater. Chem.* **2011**, *21*, 7511.
(10) Lu, Z. D.; Yin, Y. D. *Chem. Soc. Rev.* **2012**, *41*, 6874.
(11) Zhang, Q.; Liu, S. J.; Yu, S. H. *J. Mater. Chem.* **2009**, *19*, 191.
(12) Wang, G.; Peng, Q.; Li, Y. *Acc. Chem. Res.* **2011**, *44*, 322.
(13) Feng, W.; Sun, L.; Zhang, Y.; Yan., C. *Coord. Chem. Rev.* **2010**, *254*, 1038.
(14) Li, C. X.; Lin, J. *J. Mater. Chem.* **2010**, *20*, 6831.
(15) Wang, X.; Zhuang, J.; Peng, Q.; Li, Y. D. *Inorg. Chem.* **2006**, *45*, 6661.
(16) Yang, J.; Zhang, C. M.; Li, C. X.; Yu, Y. N.; Lin, J. *Inorg. Chem.* **2008**, *47*, 7262.
(17) Jia, G.; You, H. P.; Yang, M.; Zhang, L. H.; Zhang, H. J. *J. Phys. Chem. C* **2009**, *113*, 16638.
(18) Jiang, X. C.; Sun, L. D.; Feng, W.; Yan, C. H. *Cryst. Growth Des.* **2004**, *4*, 517.
(19) Li, Y. P.; Zhang, J. H.; Zhang, X.; Luo, Y. S.; Lu, S. Z.; Ren, X. G.; Wang, X. J.; Sun, L. D.; Yan, C. H. *Chem. Mater.* **2009**, *21*, 468.
(20) Dong, Q. Z.; Wang, Y. H.; Wang, Z. F.; Yu, X.; Liu, B. T. *J. Phys. Chem. C* **2010**, *114*, 9245.
(21) Xu, Z. H.; Li, C. X.; Cheng, Z. Y.; Zhang, C. M.; Li, G. G.; Peng, C.; Lin, J. *CrystEngComm* **2010**, *12*, 549.
(22) Thakur, J.; Dutta, D. P.; Bagla, H.; Tyagi, A. K. *J. Am. Ceram. Soc.* **2012**, *95*, 696.
(23) Jia, G.; Zhang, C.; Wang, C.; Liu, L.; Huang, C.; Ding, S. *CrystEngComm* **2012**, *14*, 579.
(24) Wang, X.; Li, Y. D. *Angew. Chem., Int. Ed.* **2002**, *41*, 4790.
(25) Shen, S. L.; Wang, X. *Chem. Commun.* **2010**, *46*, 6891.
(26) Chen, L. M.; Liu, Y. N.; Lu, Z. G.; Zeng, D. M. *J. Colloid Interface Sci.* **2006**, *295*, 440.
(27) Chaudhuri, R. G.; Paria, S. *J. Colloid Interface Sci.* **2010**, *343*, 439.
(28) Wang, M.; Gao, Y. F.; Dai, L.; Cao, C. X.; Guo, X. H. *J. Solid State Chem.* **2012**, *189*, 49.
(29) Xia, X. H.; Zeng, J.; Oetjen, L. K.; Li, Q. G.; Xia, Y. N. *J. Am. Chem. Soc.* **2012**, *134*, 1793.
(30) Liu, Y. S.; Tu, D. T.; Zhu, H. M.; Li, R. F.; Luo, W. Q.; Chen, X. Y. *Adv. Mater.* **2010**, *22*, 3266.
(31) Zeng, Y. B.; Li, Z. Q.; Wang, L. M.; Xiong, Y. J. *CrystEngComm* **2012**, *14*, 7043.
(32) Judd, B. R. *Phys. Rev.* **1962**, *127*, 750.
(33) Ofelt, G. S. *J. Chem. Phys.* **1962**, *37*, 511.